Inductive Probe Measurements during Plasmoid Acceleration in an RMF Thruster

Christopher L. Sercel*, Tate M. Gill †, and Benjamin A. Jorns‡
University of Michigan, Ann Arbor, MI, 48109

The induced magnetic fields and plasma currents in a rotating magnetic field (RMF) thruster are experimentally investigated. A 5 kW-class test article with RMF frequency 415 kHz is tested at a 155 Hz pulse rate, using a steady flow rate of 45 sccm Xenon propellant with pulse widths of 125 μs and a steady magnetic bias field of 180 G peak centerline strength. A clear field reversed configuration (FRC) plasmoid is observed to form and accelerate axially to roughly 2000 m/s, and peak azimuthal plasma currents of 2500 A are measured. It is found that the calculated Lorentz force accounts for ~64% of measured thrust at this operating condition. Of the Lorentz thrust, ~80% is due to plasma currents interacting with the applied magnetic bias field, while the remainder is due to mutual inductance interaction between the plasma and nearby conductive structural elements. The plasma current interacting with its own self-induced magnetic field directly produces no net axial force, but does contribute to the overall radial pressure balance in the FRC plasmoid.

I. Nomenclature

B	=	Magnetic field
ω	=	Rotating magnetic field rotational frequency
E	=	Electric field
v	=	Velocity
n	=	Density
F	=	Force
j	=	Current density
μ_0	=	Vacuum permeability
g	=	Current density scaling factor
ϵ	=	Induced EMF
β	=	Calibration transfer function
A	=	Area
V	=	Voltage
α	=	Helmholtz pair centerline field strength per unit current
I	=	Current
$\mathcal{E}$	=	Elliptic integral of 2nd kind
K	=	Elliptic integral of 1st kind
κ	=	Elliptic integral argument
P	=	Pressure
T	=	Temperature

II. Introduction

The Rotating Magnetic Field (RMF) thruster is an example of an inductive pulsed plasma thruster (IPPT), which employs a rotating magnetic field to induce an azimuthal current in a plasma. This current interacts with the radial component of a steady bias magnetic field, resulting in an axial body force on the plasma, ejecting the propellant as a

*PhD Candidate, Department of Aerospace Engineering, AIAA Student Member
†PhD Candidate , Department of Aerospace Engineering, AIAA Student Member
‡Associate Professor, Department of Aerospace Engineering, AIAA Associate Fellow

slug and generating impulse. As an IPPT, the RMF thruster shares many of its potential strengths with other in-family devices [1]. These include high throttlability while maintaining efficiency and specific impulse; high specific power [2]; and in-situ resource utilization (ISRU). [3]. The RMF current drive scheme has the additional benefit that the induced plasma current depends on the rotational frequency of the RMF rather than its magnitude [4], as is the case for other more canonical IPPTs [5]. The RMF thruster can thereby avoid the very large current and voltage transients required for other IPPTs to operate which make power supply design challenging, especially in light of switching circuit longevity.

Because of the RMF thruster's potential advantages, several groups have investigated the technology. Foremost among these studies was the work by MSNW LLC and the University of Washington with their Electrodeless Lorentz Force (ELF) thruster, which operated using nitrogen, air, oxygen, and xenon propellants in burst operation at between 10 and 70 Joules per pulse with an RMF rotational frequency of 300 kHz. [6]. Because the burst operation precludes standard thrust stand measurement, MSNW and UW measured thruster performance indirectly with a ballistic pendulum to calculate per-shot impulse and infer efficiency of up to ~ 8% [7]. This group also performed pathfinding demonstrations to show the thruster was capable of ISRU-capability [8]. More recently, the Furukawa group has developed a test unit, and they have performed electrical and plasma-based measurements. This group also used a ballistic pendulum downstream of the thruster to estimate performance, with thrust measurements peaking at ~7 mN for 3 kW operation, using 60 sccm Argon propellant flow rate with an RMF frequency of 700 kHz for a total efficiency of ~0.5% [9][10]. Furukawa's group have also performed azimuthal plasma current measurements directly using data from Hall effect probes to measure induced magnetic field gradients. They found the DC azimuthal currents induced by the RMF to be roughly 2.5% of what is theoretically expected, even for operating conditions which should result in full field penetration [11]. At the University of Michigan, we also have investigated RMF-FRC thrusters. In a recent work, we took performance measurements on a test unit known as the PEPL RMFv2. The RMFv2, whose design is detailed further in Section IV, employs power circuitry which leverages the RMF antenna as an inductor to create a series LC resonator, allowing us to pulse high oscillating currents at constant amplitude only limited by the real resistance of the circuit. We supplied ~3 kW of power, delivering up to 2.5 kA peak-to-peak RMF currents at a frequency of ~400 kHz. Xenon propellant flow ranged between 15 and 60 sccm. At these conditions, we performed the first published, direct performance measurements on an RMF thruster of which we are aware. Overall efficiency peaked at ~ 0.5% despite > 50% coupling of energy into the plasma [12]. This indicated either a very inefficient acceleration mechanism or that energy was coupling directly into irrecoverable thermal energy rather than plasma current. To investigate this, Gill et al followed this study with an efficiency breakdown based on plasma probing techniques including Faraday and Langmuir probing, retarding potential analyzer measurements, and RMF waveform analysis [13]. Gill found that the sum of thermal and magnetic energy contained in the plasma at any given time was significantly less than anticipated by performing energy coupling calculations, implying that energy was being lost after coupling to the plasma but before it could be used for thrust generation. Chief among the loss mechanisms proposed were radiation loss due to excitation collisions, and thermal losses owing to electron flux to the thruster walls.

In addition to these loss mechanisms, it is possible that the RMF current drive mechanism, and the corresponding Lorentz force acceleration, is not behaving as intended. For example, the rotating magnetic field may not be penetrating the plasma as expected according to commonly accepted conditions. As correlational evidence of this, performance was seen to improve with increased RMF field strength despite the Jones and Hugrass field penetration limits [14] having been met, indicating the mechanism of current drive may not be fully understood. Another explanation is that current could be being driven primarily in areas without significant radial magnetic bias field presence. This question could be addressed with an understanding of the driven current distribution throughout a pulse of the RMF thruster. Further, knowledge of plasma current and associated magnetic field would allow us to estimate the Lorentz force in the thruster to determine what portion of the thrust is due to the bias field versus other inductive effects or thermal effects. In light of the critical role of the current drive mechanism in the RMF thruster, the need is apparent for plasma current density measurement to assess whether current generation and plasma acceleration behave as understood.

The goal of this work is to make magnetic field and current density measurements during pulsed operation of an RMF thruster. To that end, we organize the paper in the following way. In Section III we discuss in detail the operating principles of the RMF thruster as they are presently understood, as well as the operating principle for the proposed inductive probing technique. In Section IV, we present the experimental setup required to use these probes and collect data. In Section V we detail the analysis necessary to extract useful current density information from the raw data collected. In Section VII we discuss the physical significance of the results, and finally in Section VIII we summarize this work and conclude.

III. Principles of Operation

We begin this section by establishing the presently understood principles of operation for the RMF thruster. We discuss the mechanism by which the RMF induces plasma current and how that current can be used to generate thrust before acknowledging the major challenges for efficient operation. We follow with an explanation of the inductive probe technology used in this study and how the data can be used to illuminate the plasmoid formation process.

A. Thruster Operation

As shown in Figure 1, the canonical geometry of the RMF thruster consists of a plasma-bounding cone surrounded by a pair of saddle coils used to produce the RMF and one or more DC magnets used to produce the steady bias magnetic field. A seed plasma source must also be present, typically positioned at the smaller 'throat' end of the cone and flowing toward the larger 'mouth' end. Each saddle coil is shaped such that it effectively forms a Helmholtz pair with itself, with each Helmholtz loop on the opposite side of the cone. In this way, running a current through one of the saddle coils produces a uniform magnetic field orthogonal to the cone axis. By orienting each saddle coil 90 degrees from the other and running sinusoidal current through each coil 90 degrees out of phase from the other, their magnetic fields can be superposed to result in a field transverse to the axis of the cone whose direction rotates with the same frequency as the input current sine waves. Finally, the DC bias magnets are typically electromagnets. The magnitudes of the current through each electromagnet can be tuned to produce the desired field shape such that the field is tangent to the plasma-bounding cone along the walls.

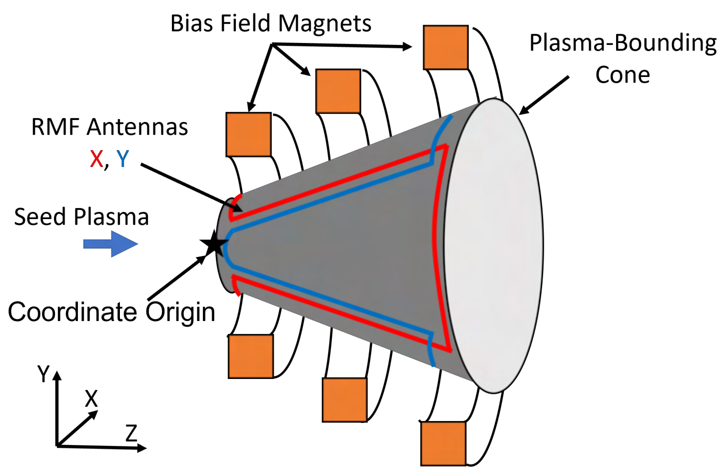

Fig. 1 Basic geometry of the canonical RMF thruster.

1. Current Induction

The rotating magnetic field whose generation is described above can be described by

$$\vec{B}_{RMF} = |B_{RMF}| \left(\cos(\omega t)\hat{x} + \sin(\omega t)\hat{y}\right), \tag{1}$$

where ω is the RMF frequency and where the coordinates x and y match the convention established in Figure 1. Applying Faraday's Law to this expression results in the following induced axial electric field:

$$\vec{E} = \omega \, |B_{RMF}| \left(x \cos(\omega t) + y \sin(\omega t)\right) \hat{z}. \tag{2}$$

For the simplest case, we assume the cone is already filled with a plasma of non-inertial, collisionless electrons and cold, unmagnetized ions. For these conditions, Ohm's Law reduces to the form

$$\vec{E} = -\vec{v}_e \times \vec{B}, \tag{3}$$

where $\vec{v}_e$ is electron velocity. Substituting Equations 1 and 2 into Ohm's law, we find that the electron velocity must be given by

$$\vec{v}_e = \omega\left(-y\hat{x} + x\hat{y}\right) = \omega r\hat{\theta}, \tag{4}$$

so that we can arrive at the current density

$$\vec{j} = -en_e\omega r\hat{\theta}. \tag{5}$$

Significantly, we note that j does not depend on the magnitude of B, which we mentioned as a potential strength of this current generation mechanism in Section II. In reality, induced currents, collisionality, and thermal effects combine to screen out the RMF and thus change $\vec{B}_{RMF}$ from its ideal form in Eq. 1. To combat this, so-called penetration requirements have been proposed, which establish the minimum RMF field strength required to keep Eq. 5 approximately valid [15].

While this analysis assumes plasma is already present in the thruster before the RMF is pulsed, the RMF is a prolific ionizer and this process requires only a seed plasma. In our case, a LaB_6 hollow cathode produces a seed plasma of roughly 1-3% overall ionization fraction before the RMF is pulsed.

2. Thrust

The azimuthal current generated by the RMF can now be leveraged to produce thrust via Lorentz force interaction with a radial magnetic field. This force is given by

$$F = \iiint_V B_r j_\theta d^3r, \tag{6}$$

where B_r refers to the radial component of the magnetic field, d^3r is the differential volume element, and V refers to the volume of space wherever plasma exists. While a large component of this magnetic field is generated by the DC bias magnets, the transient currents in the plasma will give rise to additional induced magnetic field B_{ind} such that $\vec{B} = \vec{B}_0 + \vec{B}_{ind}$. Further, the induced magnetic fields can result from two main sources which we will refer to in this work as the self field $\vec{B}_{self}$ and the structure field $\vec{B}_{struct}$. The self field as we define it here results directly from the currents in the plasma. The structure field, meanwhile, is caused by mutual inductance between the plasma and any conductive structural element on or near the thruster. As current is generated in the plasma, this mutual inductance will cause coupled currents to form in nearby conductive elements. Those transient currents in the thruster's structure will, in turn, induce the structure field.

The ability of the induced magnetic field to produce net thrust is primarily thought to be a consequence of secondary interactions with other conducting surfaces enclosing the plasma [1], or in other words the structure field. Because the structure magnetic field is induced by transients in the plasma currents, it is be described by Faraday's Law of induction, which states

$$V_2 = \frac{d}{dt}\left(M_{1,2}I_1\right) \tag{7}$$

where $M_{1,2}$ is the mutual inductance between elements 1 and 2, V_2 is an induced voltage, and I_1 is a current. In the simplified case that the secondary winding has negligible inductance and capacitance, $I_2 \propto \frac{dI_1}{dt}$. With these assumptions and considering the structure field is due to currents induced on secondary elements by the plasma currents,

$$\vec{B}_{struct} = \vec{\gamma}\left(\vec{r}, t\right)\frac{d}{dt}\iiint_V j_\theta d^3r, \tag{8}$$

where $\vec{\gamma}$ is a proportionality factor which encapsulates the mutual inductance between the plasma and any conductive structural elements. While Eq. 28 is a vast simplification, it serves to illustrate that the magnitude of the structure field is dependent on geometric factors as well as the rate of change of the induced plasma currents.

The plasma will also experience force from its own self field, which is given by the Biot-Savart law as

$$\vec{B}_{self} = \frac{\mu_0}{4\pi} \iiint \frac{\vec{j}(\vec{r}') \times \vec{r}'}{|\vec{r} - \vec{r}'^3|} d^3 r', \tag{9}$$

where r' is a dummy variable integrated over all space and j is the plasma current. It is possible that due to the axial asymmetry of the thruster's conical geometry, the net self-field force will be nonzero in the axial direction. However, we make the argument that this net axial force should be zero. Conservation of momentum requires that any forces on the plasma be balanced, and without interaction with a fixed object, the plasma should not be able to cause acceleration of its own center of mass. This being said, we expect that radial forces should not necessarily be zero as radial expansion and contraction does not require the center of mass to accelerate.

We now present the total force on the plasma due to the three sources of magnetic field: bias, structure, and self. For clarity, we make the additional substitution that $\vec{j} = I_\theta \vec{g}$, whereby we separate the magnitude of the azimuthal current I_θ and a function $\vec{g}$ which describes its spatial distribution. In this case, we can perform substitution to Eq. 6 to arrive at the expression

$$F = \iiint_V \left(I_\theta g_\theta B_{0r} + I_\theta \frac{dI_\theta}{dt} g_\theta \frac{d}{dt} \iiint_V g_\theta d^3 r + \frac{\mu_0}{4\pi} I_\theta^2 g_\theta \iiint_V \frac{\vec{g}(\vec{r}') \times \vec{r}'}{r'^3} \right) d^3 r', \tag{10}$$

which can be integrated again over time to calculate the impulse per shot. Eq. 10 shows linear force scaling with the induced current magnitude in the leftmost term which describes bias field interaction, but quadratic scaling in the middle and rightmost terms which describe structure and self-field interractions. This quadratic scaling is key to the high specific powers which inductive pulsed plasma thrusters can reach, and why they are uniquely suited to pulsed operation. We can also clearly see thrust does not depend on the RMF amplitude as mentioned previously, allowing the RMF thruster to operate with gentler voltage and current transients than other inductively-driven pulsed thrusters.

B. Probe Operation

The basis of the inductive probing techniques used in this study is Faraday's Law, which states

$$\vec{\nabla} \times \vec{E} = \frac{\partial \vec{B}}{\partial t}. \tag{11}$$

Given a wire loop, we can integrate over the area enclosed by the wire loop. Applying Green's theorem to the left-hand side yields he relation

$$\epsilon = -N \frac{\partial \Phi}{\partial t} \tag{12}$$

$$= -NA\dot{B}, \tag{13}$$

where Φ is the flux integral of the magnetic field through the wire loop and ϵ is an induced EMF. We have also multiplied the induced EMF by the number of turns N in the case of a multi-turn loop. In the second line, we have made the further assumption that the strength of the changing magnetic field does not vary significantly over the length scale of the wire loop's diameter. By integrating Eq. 13, we are able to directly measure the magnetic field as a function of time at the location of our wire loop. In reality, this process requires additional calibration to eliminate frequency-dependent effects such as capacitance and inductance in the measurement circuit which can cause amplification or time-delay of certain frequencies. This calibration process is described in detail in Section V.

IV. Experimental Setup

As the objective for this study is to characterize the magnetic field environment inside the RMF thruster during plasmoid acceleration, the thruster must be run in a fashion representative of actual operation. In the following section, we describe the test facility, thruster, and probes used to collect the data.

A. Test Facility

This study was conducted in the Large Vacuum test Facility (LVTF) at the University of Michigan's Plasmadynamics and Electric Propulsion Laboratory, depicted in Figure 2b. LVTF is a 6×9 meter chamber, with cryopumping surfaces capable of pumping up to 600,000 L/s X [16]. For this study, not all pumps were used, resulting in non-operating base pressures of approximately 2×10^{-7} Torr and operating pressures of approximately 5×10^{-6} Torr as measured by a Stabil ion gauge situated in the exit plane of the thruster and 1 meter to the side. The thruster was situated approximately 3 meters from a graphite beam dump. A multitude of feedthroughs and viewports allowed for high power connections to conduct current to the RMF antennas, and observation of the thruster though both traditional and high-speed photography. Other diagnostics included the inductive probes discussed in this sutdy as well as a thrust stand, various plasma probes, and current measurement to the RMF antennas. RMF current measurment was performed using Pearson coils, and high-speed video which is critical for thruster health diagnosis was taken at 50 kHz both from a side view and a straight-on view.

B. Thruster Under Test

As the goal of this work is to investigate the physics of the RMF thruster, we have designed and built a test article which attempts to follow heritage from previous designs. A detailed discussion of the design process based on presently understood scaling laws can be found in Sercel et al., 2021 [12]. Based on previous analytical work, the thruster is constructed as much as possible from non-conductive materials to avoid stray coupling of the RMF [17]. The major components of the thruster include the seed ionization source and flow system, the plasma-bounding cone, the RMF antennas and power lines, and the bias magnets. A closed loop chiller supplies cold water to maintain temperature for the thrust stand and the RMF antennas. Figure 2a shows a photograph of the test unit, named the PEPL RMFv2.

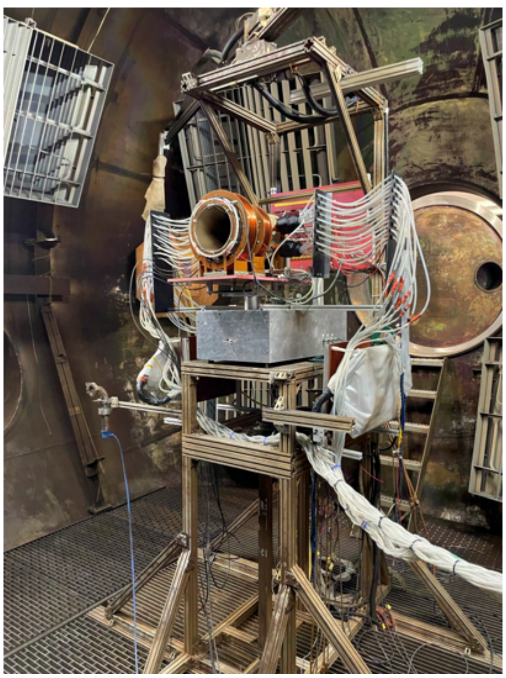

(a)

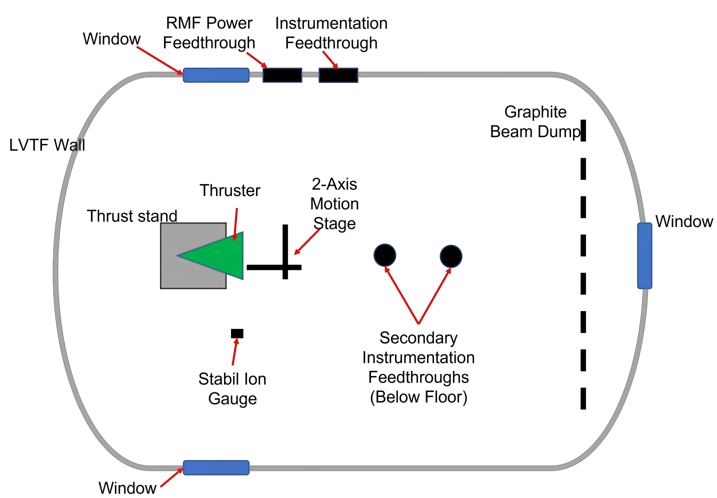

(b)

Fig. 2 Overview of the test setup in the Large Vacuum Test Facility at the University of Michigan. a) Photograph of the PEPL RMFv2 on its thrust stand. b) Top-down diagram of chamber configuration.

Due to institutional familiarity, a LaB_6 hollow cathode was chosen to act as the seed ionization source. Using xenon as propellant, this cathode discharged to a stainless steel anode approximately 6 cm in diameter at a current of 18 A and a flow rate of 15 sccm Xe. The remainder of the propellant required to achieve a given operational setpoint was flowed through the neutral diffuser. The neutral diffuser consists of a stainless steel tube situated at the exit plane of the thruster following the circumference of the plasma-bounding cone, with pinholes to diffuse and direct the flow upstream for greater residence time. While the use of a LaB_6 cathode limits us to noble gas operation, which is not fundamentally required by this thruster's architecture, the choice allows us to leverage existing expertise and focus on RMF thruster physics rather than the engineering challenges of developing an alternative ionization source.

Situated directly downstream of the anode is the plasma-bounding cone. This cone is constructed of a scaffold of G10 fiberglass supporting a sheet of flexible mica. The cone measures approximately 6 cm in diameter at the narrow 'throat' end and 20 cm at the wider 'mouth' end, with total length of 33 cm for a half angle of approximately 12 degrees.

Wrapped directly around the plasma-bounding cone, the RMF antennas consist of 0.25" copper tubing so that they can be directly water cooled to maintain constant resistance during operation. They are insulated with EPDM rubber tape, which is necessary to hold off the ~15 kV potential swing they experience during thruster operation. To minimize the line inductance, the RMF cables for each antenna consist of 10 separate lines for each polarity which are inter-braided to reduce their self-inductance. To facilitate the connection of 10 conductors to each end of each antenna, we use high-current connectors which are designed for underwater use, which we seal with silicone caulk to provide additional insulation. The presence of high density plasma so close to these very high voltage conductors make insulation a challenge which must be taken seriously, as a plasma-antenna short necessitates a chamber vent cycle to address.

To produce the ~415 kHz, multi-kA oscillating current we need to produce the RMF, we have partnered with Eagle Harbor Technologies via an SBIR grant to develop a custom power supply. A tuning capacitor bank is situated in the chamber as close as possible to each antenna to form a series LC resonator. This LC circuit is then pulsed by our supply at resonance, delivering a pulse of desired length with constant maximum amplitude limited only by the real resistance of the circuit. This highly enabling supply is limited to approximately 4 kW operation.

C. Probe Construction

The B-dot probes used were constructed according to the principles laid out in the best practices paper by Polzin et al., 2017 [18]. Figure 3 shows the probe used in this work. Fiberglass rod was used as a heat resistant, nonconductive bobbin material. Space for the 24 AWG enameled copper wire was machined out using a lathe, and turns were applied over a 0.25" length between radii of 0.25" and 0.5" for both the axial and radial probes. The radial probe bobbin was attached to the axial probe resulting in a measurement offset of 0.125" both radially and axially. To minimize the effect of stray electrical noise, the wire leads were tightly twisted and adapted to grounded coaxial cable as close to the windings as possible, with the connection point insulated using shrink tubing and silicone electrical tape. A pyrex glass test tube was fit snugly over the entire probe apparatus to protect the enameled wire from the plasma but not fully sealed at the back end to prevent unwanted pressure differential across the tube during vacuum operation. This two-axis probe setup was mounted to a two-axis motion stage to sweep the axial and radial dimensions of the interior of the plasma-bounding cone.

Fig. 3 Photograph of 2-axis B-dot probe used in this study.

Because of the ~2 kA oscillating currents associated with the RMF, significant 415 kHz noise exists in the vicinity of the thruster. The expected B-dot full-scale signal is on the order of 500 mV, while the RMF directly induces several 10s of volts of signal. This signal is due to direct coupling between the probe and its cabling and the antennas as it exists unchanged whether plasma is present or not. To combat this, we employ physical low-pass filters in-line with the probe. These 3rd-order RC filters have a cutoff frequency of 100 kHz and attenuate the 400 kHz component of the signal. Because we are interested in currents being generated across time periods of 10s of μs, the content we are concerned with exists primarily below 100 kHz. Therefore this cutoff frequency is acceptable and allows us to set full-scale measurement range much closer to the full-scale signal for better measurement resolution.

The B-dot probes themselves must also be calibrated as mentioned in Section III. This calibration is achieved using an off-the-shelf Helmholtz pair which produces a constant magnetic field near centerline of 7.433×10^{-4} Tesla per amp, verified via a LakeShore MMZ-2508-UH Hall probe. The calibration is done in-place and with all the final cabling to ensure that stray inductance and capacitance are representative of the test setup. With the B-dot probe installed, the Helmholtz pair is situated such that the probe is coaxial and centered. A signal generator produces a sin wave at a desired frequency, which is amplified to produce a higher current and therefore higher calibration signal. This amplified signal is passed to the Helmholtz pair, and the current passing to the pair is measured via a Model 6585 Pearson coil while the voltage on the probe is simultaneously measured. This allows us to relate the voltage response of the probe to the rate of change of magnetic field at a given frequency. This process is repeated at 5 kHz intervals from 1 kHz to 400 kHz, though calibration content above ~120 kHz is nearly fully attenuated by the in-line low-pass filter. Data was captured using an Alazar ATS9462 virtual oscilloscope operating at a collection frequency of 5 MS/s.

D. Operating Points

The RMF thruster has several operational variables which can be adjusted parametrically to change thruster behavior without any physical reconfiguration. To facilitate understanding of the scaling and trends which the thruster exhibits, we have taken this inductive probing data at a range of operating points. For the measurements presented in this work, the thruster was operated at a steady flow rate of 45 sccm Xe, while the RMF was pulsed at 2000 A peak-to-peak for 125 μs pulses at a repetition rate of 155 Hz. This operating point was chosen because it resulted in one of the highest total efficiencies observed across a recent performance study whose results are yet unpublished at the time this publication. The bias magnetic field was operated such that the maximum centerline field strength was 180 G at a location 5 cm upstream of the cathode exit plane. The 2-axis B-dot probe was swept in a grid pattern through an axial-radial cross-section of the thruster with grid spacing 2 cm. To ensure that the data represented typical behavior, a total of 100 pulses were captured for each location, and the resulting probe traces were averaged before final analysis.

V. Analysis Methodology

Before examining the raw data collected during thruster operation, we must perform several additional steps of analysis. As mentioned previously, the raw B-dot data must be processed using a frequency-dependent calibration to remove time delay and ensure correct magnitude. We then use the processed B-dot data to calculate current density in the thruster, and finally thrust by combining the current and magnetic field measurements. The methodology behind these analyses is discussed in this section.

A. Probe Calibration

As discussed in Section IV.C, the B-dot probes used in this study require a frequency-dependent calibration to eliminate the effects of any capacitance and inductance which could alter the signal. In this case, the calibration is even more necessary as a low-pass filter was used to reduce the impact of the RMF on the B-dot signal to a manageable level.

The calibration takes the form of a probe-specific, frequency-dependent transfer function $\beta(f)$ such that

$$\beta = \frac{\text{FFT}\left(V_p\right)}{\text{FFT}\left(\dot{B}_{cal}\right)} \tag{14}$$

$$= \frac{\text{FFT}\left(V_p\right)}{\text{FFT}\left(\alpha \dot{I}_{cal}\right)} \tag{15}$$

where V_p is the voltage read from the probe and $\dot{B}_{cal}$ is the known externally applied magnetic field for calibration purposes, generated in our case by a Helmholtz pair. We have also made the further substitution that $B_{cal} = \alpha I_{cal}$ where I_{cal} is the measured current injected into the calibration Helmholtz pair, and α is a constant which describes the magnetic field produced per amp at centerline.

For probing applications in which meaningful content is expected to exist at a single frequency, β can be calculated by injecting an I_{cal} which oscillates at that frequency. However, for a wide-band application in which the response is not necessarily expected to be constant with frequency, as is the case here due to long cables and in-line filters, β must be calculated at all frequencies of interest. In this case, given the 100 kHz corner frequency of the low-pass filters used, we require values of β up to approximately 100 kHz.

To compute our specific β for each probe, we injected current oscillating at a pure sine wave at a specified frequency ω_{test} into the Helmholtz pair. The value of this current and the corresponding voltage signal is collected using an oscilloscope. These two signals are then Fourier transformed, and the complex-valued content associated with ω_{test} is extracted and divided according to Eq. 15. The result of this process is $\beta(\omega_{test})$. This process is repeated at 5 kHz intervals between 1 kHz and 100 kHz, and a spline is fit to the complex result. The transfer function for each probe can be seen in Figures 4a and 4b.

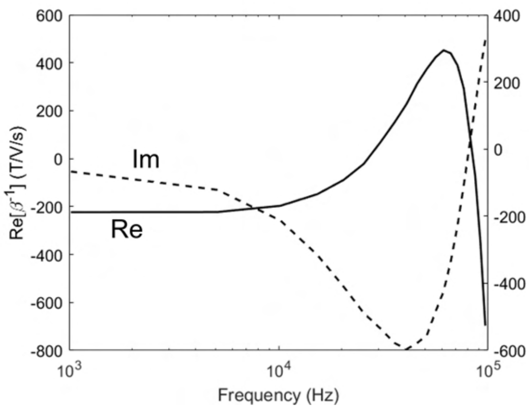

(a) Axial Probe

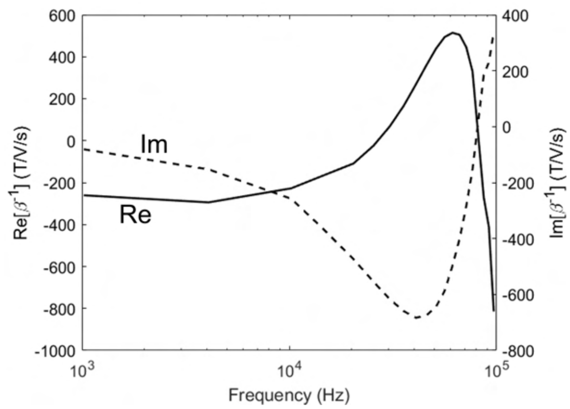

(b) Radial Probe

Fig. 4 Transfer function for both B-dot probes over relevant frequency range.

Once the full range of β is calculated, we can extract our meaningful result by applying

$$\dot{B} = \mathrm{IFFT}\left(\frac{\mathrm{FFT}\left(V_p\right)}{\beta}\right). \tag{16}$$

Finally, the signal can be integrated to arrive at $B(t)$.

B. Current Density and Force

Once calibration is complete, we are left with a map of $\vec{B}(r, z, t)$. With the complete value of the magnetic field in-hand, we can compute the current through Ampere's Law, which states in its differential form:

$$\vec{\nabla} \times \vec{B} = \mu_0 \vec{j} \tag{17}$$

where μ_0 is the vacuum permeability and $\vec{j}$ is the vector-valued current density. Because the current density we are concerned with runs in the azimuthal direction, we can take the θ-component of the curl in cylindrical coordinates, which is given by

$$\left(\vec{\nabla} \times \vec{B}\right)_\theta = \frac{\partial B_z}{\partial r} - \frac{\partial B_r}{\partial z} = \mu_0 j \tag{18}$$

As discussed in Section IV, we employ a 2 cm grid for our B-dot probe measurements. To facilitate differentiation in 2 dimensions, we apply a 2D biharmonic spline interpolation, implemented from Sandwell, 1987 [19] with a 0.5 cm spacing. The Sandwell interpolation algorithm was used over MATLAB's built-in interp2 algorithm because of its friendliness toward non-uniform data spacing, as the shape of the thruster cone required the data not to be spaced a uniform rectangular grid.

Once the current map at a given instant is computed, the Lorentz force on the plasma can be estimated by multiplying the current by the magnetic field. Specifically,

$$F_z = 2\pi \int \left(B_{r,bias}(r,z) + B_{r,self}(r,z,t)\right) j(r,z,t) r dr dz \tag{19}$$

$$F_r = -2\pi \int \left(B_{z,bias}(r,z) + B_{z,self}(r,z,t)\right) j(r,z,t) r dr dz \tag{20}$$

where we have included both the effect of the steady bias field and the self-induced field on the total force.

C. Self Field

As discussed in Section III, we assume that the magnetic field capable of producing a Lorentz force in the plasma stems from three separate sources of current: the bias field is generated by the steady bias electromagnets; the self field is generated directly by the currents induced in the plasma itself; and the structure field is induced in structural elements surrounding the plasma due to mutual inductance between those structures and the plasma. We wish to separately identify these magnetic fields to attribute Lorentz force to each source individually.

Identifying the bias field is trivial, as it does not contribute to B-dot measurements owing to its steady nature. No analysis is required to separate it from the other field sources. To calculate the total field structure, we superpose the bias field on any measurements from inductive probing.

We define the self field as the magnetic field arising due directly to the plasma currents. Therefore, to calculate the self field, we begin at a given time stamp with the current density from Eq. 5 and apply the Biot-Savart Law found in Eq. 9. Because calculating the magnetic field at a given point requires integration over all space, we can reduce calculation time by employing the analytic solution to the Law of Biot-Savart for a discrete wire loop with its center situated at $r = 0, z = 0$.

$$B_r(r,z) = \frac{\mu_0 I z \left(\left(R_L^2 + r^2 + z^2\right)\mathcal{E}(\kappa) + R_{min}^2 K(\kappa)\right)}{2\pi R_{min}^2 R_{max} r} \tag{21}$$

$$B_z(r,z) = \frac{\mu_0 I \left(\left(R_L^2 - r^2 - z^2\right)\mathcal{E}(\kappa) - R_{min}^2 K(\kappa)\right)}{2\pi R_{min}^2 R_{max} r}, \tag{22}$$

where r and z are the coordinates of the measurement location, R_L is the radius of the current loop, I is the current flowing through the loop, K and $\mathcal{E}$ are elliptic integrals of the first and second kind respectively, and the intermediary parameters R_{min}, R_{max}, and κ are given by

$$R_{min} = \sqrt{z^2 + (r - R_L)} \tag{23}$$

$$R_{max} = \sqrt{z^2 + (r + R_L)} \tag{24}$$

$$\kappa = \frac{4 r R_L}{R_{max}^2}. \tag{25}$$

Because of the discrete nature of the data, it is straightforward to discretize the current density map into individual points and convert to current by multiplying by the area subtended by each measurement location throughout the cone. The contributions to the magnetic field at a point of interest by each plasma current loop are then calculated via Eqs: 21 and 22 and summed over to produce a map of the magnetic field directly induced by all the measured azimuthal plasma currents. Written analytically,

$$B_{self,r}(r,z) = \sum_{r',z'} \frac{\mu_0 I(r',z') z \left(\left(r'^2 + r^2 + (z-z')^2\right)\mathcal{E}(\kappa) + R_{min}^2 K(\kappa)\right)}{2\pi R_{min}^2 R_{max} r} \tag{26}$$

$$B_{self,z}(r,z) = \sum_{r',z'} \frac{\mu_0 I(r',z') \left(\left(r'^2 - r^2 - (z-z')^2\right)\mathcal{E}(\kappa) - R_{min}^2 K(\kappa)\right)}{2\pi R_{min}^2 R_{max} r}, \tag{27}$$

where we recognize that R_{min}, R_{max}, and κ are functions of r' and z', though it is not explicitly notated.

D. Structure Field

In the case that all currents strong enough to produce a measurable field have been accounted for when calculating the self field via Eqs. 26 and 27, then the originally measured magnetic field $\vec{B}_{meas}$ and the self field $\vec{B}_{self}$ will be exactly equal. However, if there are sufficiently strong currents outside the bounds of the plasma, these will result in a nonzero difference between $\vec{B}_{meas}$ and $\vec{B}_{self}$. Under the assumption that plasma currents exist solely in the cone of the thruster where we probed, any remaining field not explained by $\vec{B}_{self}$ must then be due to transient currents induced in conductive structural elements such as the bias electromagnets. Therefore, we can calculate $\vec{B}_{struct}$ by taking

$$\vec{B}_{struct} = \vec{B}_{meas} - \vec{B}_{self} \tag{28}$$

It may be noted that the structure field as calculated in this manor could have contributions due to plasma currents in the plume, outside the region of interrogation. However, the magnetic field induced by these external plasma currents would have a direction opposite to what is expected and observed from the structure field in this formulation. We therefore recognize that this is a conservative estimate of the magnitude of the structure field.

VI. Results

In this section we present the results for our inductive probing of the RMF thruster during operation. We first show images of the field shape directly captured using the B-dot probes, then present the necessary plasma currents required to produce those field shapes. Finally, we show the thrust values calculated from applying the Lorentz force to the measured current and magnetic fields, separating axial force into contributions by the bias, self, and structure magnetic fields. All results shown are for thruster operation at 2 kA peak-to-peak RMF current with RMF frequency 415 kHZ, operating at a pulse rate of 155 Hz and pulse duration of 125 μs with a steady flow of 45 sccm Xe. Bias magnetic field was set to 180 G peak centerline field strength.

A. Induced Field Measurements

Figure 5 displays the net magnetic field in the RMF thruster at several time steps. These field lines are the summation of the steady bias magnetic field and the induced magnetic field measured using our B-dot probe sweep. Although we have only probed the induced field inside the cone of the thruster, we wish to present a zoomed out view to more effectively illustrate plasmoid formation. To accomplish this, the induced field outside the cone in Figure 5 is purely due to the self field, which can be calculated at any arbitrary point using Eqs. 26 and 27, while the field inside the cone is the full, directly measured magnetic field which includes both the self field and structure field contributions. A slight discontinuity can be observed at the exit plane at the 140 μs time step because of this, though by this time the RMF pulse has ended and induced forces are small, as seen in Figure 8b.

We observe that before the mass ionization event seen at ~70 μs into the pulse, the bias field remains relatively undisturbed. After the ionization event, we see a dramatic shift as the field close to centerline reverses and a magnetic separatrix forms. This separated field structure begins axially long, taking up nearly the entire thruster, but then translates downstream at a speed of roughly 2000 m/s as it is compressed into a more narrow, contained region. We note that the plasmoid seems to remain relatively stationary at the lip of the thruster for several 10s of μs before dispersing.

B. Induced Current

After taking the curl of the induced magnetic field measurements and diving by μ_0 as discussed in Section V, we are left with the local azimuthal current density. Figure 6 shows this distribution at several timesteps, with peak current density of ~30 A/cm^2 occurring at approximately the 70 μs point. We see behavior qualitatively in line with what has already been presented in the induced magnetic field. A strong ionization event and azimuthal current spin-up occurs around 60-70 μs, followed by the current-carrying region translating downstream and experiencing reduced axial width. The current can also be seen to exist largely in the outer regions of the cone. This is consistent with the concept of electron entrainment in the RMF, in which current is expected to increase linearly with the radius as seen in Eq. 5.

As a further metric of the efficacy of the RMF current drive mechanism, we can integrate the current density from Figure 6 to produce the plot in Figure 7. Induced current can be seen to peak at a value of ~2500 A at roughly the 70 μs mark corresponding to the ionization and spin-up event seen in Figure 6, followed by a decline to the steady value of ~1100 A, where it remains until the pulse ends at the 125 μs mark. The magnitude of this current, which is greater

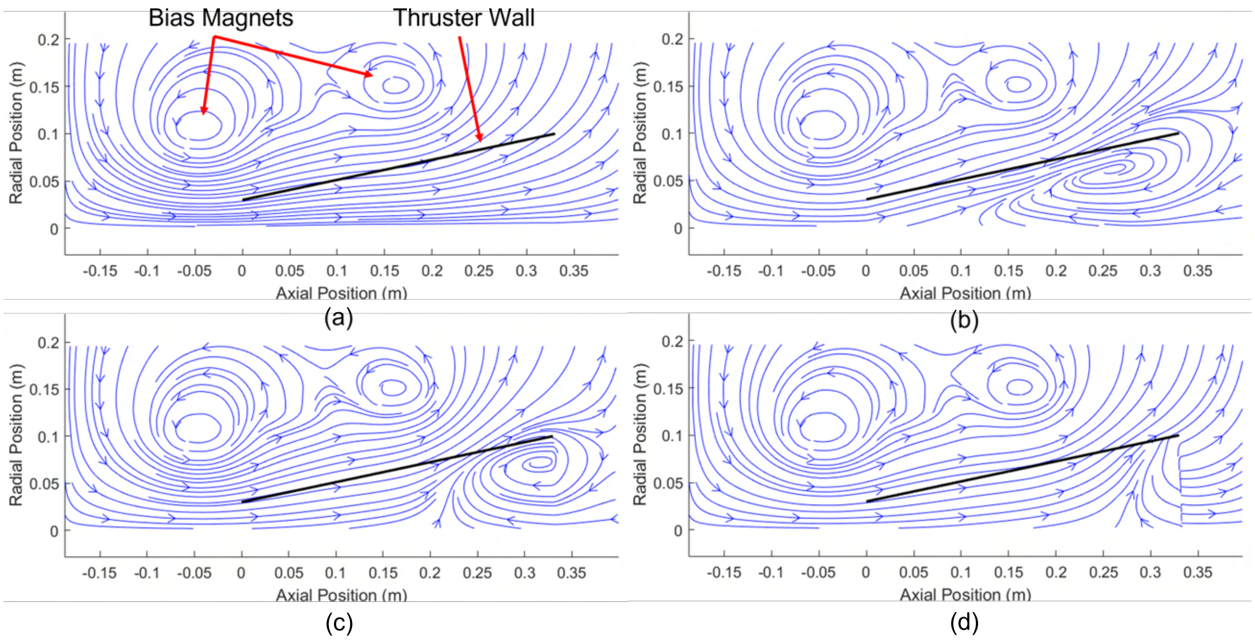

Fig. 5 Streamline plot of total magnetic field (bias and induced) in and around the RMF thruster over the pulse duration. Inside the cone a) 35 μs. b) 70 μs. c) 105 μs d) 140 μs.

than the peak-to-peak amplitude of the input RMF current, substantiates the idea that the RMF is a prolific ionizer and effective current drive mechanism. The total current can be seen to dip below zero at the end of the pulse, and briefly before the mass ionization event. We ascribe these to measurement error owing to the signal processing, spline fitting, and integration involved in producing these plots rather than actual negative currents, which we see no physical basis for.

C. Force

Per Eqs. 19 and 20, we can calculate the total force on the plasma at any given time. Figure 8a shows the axial Lorentz force experienced by the plasma over time in both the axial and radial directions. First examining the axial component of the force, we see that the force caused by pushing off the applied bias field follows a familiar shape, with a peak of ~60 mN at the 70 μs point followed by a less intense plateau of ~35 mN until the pulse ends at 125 μs, at which point the force decays. As with Figure 7, we see a negative value to the force after the pulse has ended, and we attribute this to the same sources of error as the current. Integration over time yields a net impulse of 36.3 μN-s per pulse. At 4 kW operation, our power supply allows for up to 155 Hz rep rate at this operating point for an anticipated average thrust of 5.6 mN. If we ignore the erroneous negative force after the RMF has already shut off, we instead find or impulse to be 40.3 μN-s per pulse, for a 4 kW thrust of 6.2 mN. Actual thrust stand measurement at this operating condition is 9.7±1.7 mN. Lorentz force estimates therefore capture roughly 64% of the measured thrust in the best case.

The radial force can be seen to nearly double the axial force in magnitude at the peak value. The radial impulse per shot comes to -130.6 μN-s per pulse with the data uncorrected, or -144.7 μN-s per pulse while ignoring the erroneous thrust at the end of the pulse. While this strong negative force appears to contradict the stable plasmoid depicted in Figure 5, thermal pressure in the outward direction is of similar magnitude according to yet unpublished triple Langmuir probe results by Gill et al. Taking the 100 μs time step as an example, magnetic pressure given by $P_{mag} = \frac{B^2}{2\mu_0}$ is roughly 18 Pa, while electron thermal pressure given by $n_e k_B T_e$ is roughly 12 Pa. This outward thermal pressure likely counteracts the inward magnetic pressure to produce the stable plasmoid observed.

We can examine the contributions to the useful axial force in greater detail in Figure 8b, which splits up the contribution between Lorentz interaction with the steady bias field, the self field, and the structure field. Notably, we see no contribution whatsoever from the self field, a finding which confirms our argument based on conservation of momentum and is discussed in further detail in Section VII. To see why the self field does not contribute to axial thrust, Figure 8c depicts a contour plot of the axial force density in the r-z plane captured at the 70 μs mark. In this plot, the

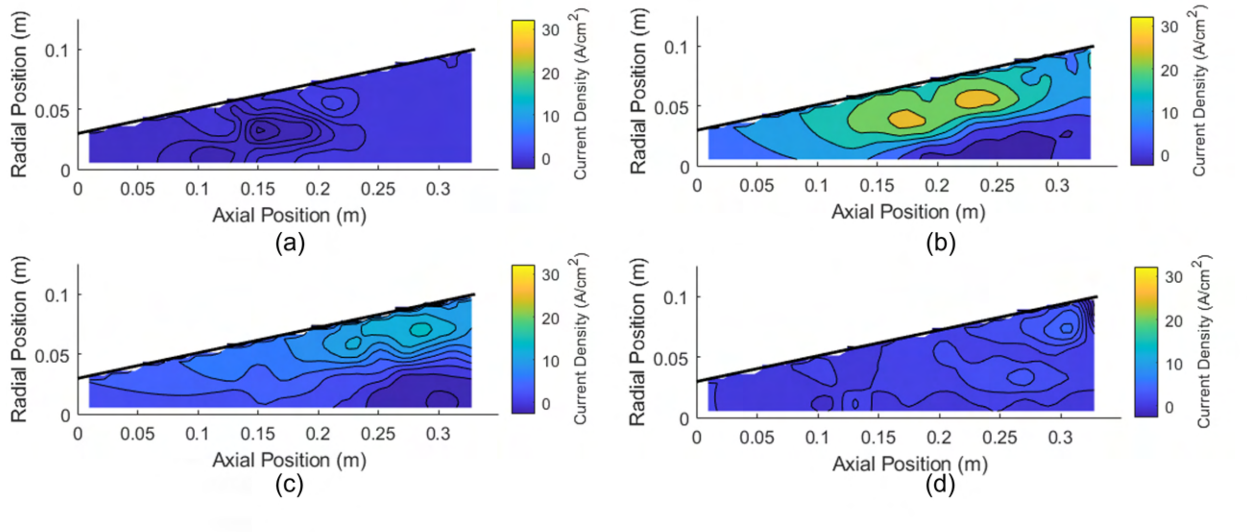

Fig. 6 Induced current density in the RMF thruster over the pulse duration. a) 35 μs. b) 70 μs. c) 105 μs. d) 140 μs.

volumetric force density has been integrated about θ but not yet r or z. We see that upstream of the plasmoid, the force is positive as the self field in this region points in the positive r direction. However, downstream of the plasmoid, the self field points toward the axis, and thus the direction of force reverses. After integration, these two forces exactly cancel each other, resulting in plasmoid compression but not net acceleration.

In contrast to the self field, the structure field contributes roughly 21% of the total impulse generated by the axial Lorentz force this thruster design minimizing major conductive elements. Its positive direction is indeed indicative of a mutual inductance between the plasma and stationary structural elements; force caused by magnetic fields induced by plasma currents not in the probe interrogation region could impact the magnitude of the structure field as calculated in the manor laid out in Section V, but they would result in a negative force. We also observe the structure force peaks roughly 50 μs after the bias force and the total induced current. A time delay here is consistent with this magnetic field being caused by a mutual inductance relationship between the plasma and other conductive elements, though the expected time scales would depend on the inductance and resistance of the elements involved.

VII. Discussion

In this section, we examine our results in the context of how the RMF thruster is presently understood. We begin with a discussion of the observed field reversal and the RMF current drive's efficacy before relating the performance results to previous measurement and conclude with our thoughts on how these results impact the future research of this thruster.

A. Field-Reversal and the RMF Current Drive

One notable result from the magnetic field streamplots of Figure 5 is the formation of a field-reversed configuration plasmoid, or FRC, during the pulse. The FRC was the orignal goal of the RMF current drive mechanism as a fusion containment device, as it leads to a relatively stable, compact plasma structure. This has been proposed to represent a possible advantage over other pulsed plasma thrusters as the FRC could increase antenna-plasma coupling by providing a relatively dense, stiff structure and thus boost efficiency [20], as well as helping to prevent wall losses by minimizing plasma-wall interaction via the FRC's containment. The FRC was not a specific goal of this device, but evidence of the structure serves to qualitatively support that the main thruster mechanisms are behaving as anticipated.

Indeed, the RMF current drive can be seen to be a highly effective current drive mechanism, as we see a peak induced current of 2500 A with an injected RMF current of 2000 A peak-to-peak. The high current we are able to drive using the RMF is due to the unique current drive mechanism which results in an ideal current density of $j = en\omega r$,

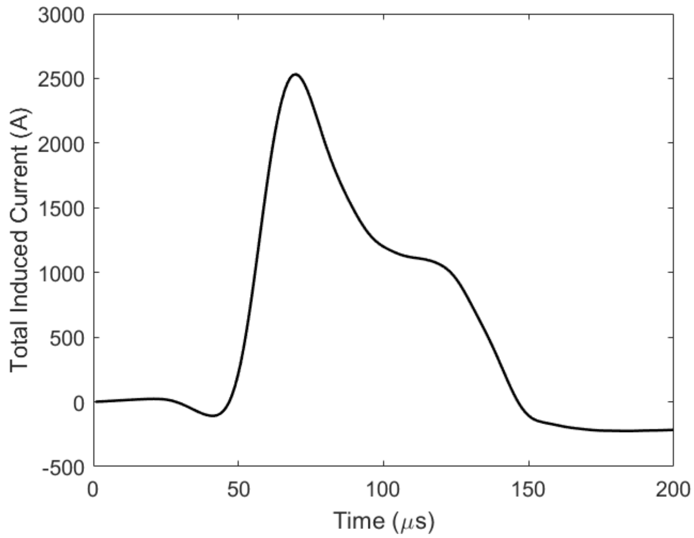

Fig. 7 Total induced current in the RMF thruster as a function of time.

allowing the driven current to scale independently of the magnitude of the RMF strength provided penetration is met. This is in contrast to a more traditional θ-pinch style inductive current drive, in which the maximum current driven in the plasma is that which causes a net zero change in magnetic flux during a pulsed current transient in a driver antenna. The major implication of the success of the RMF current drive scheme is that azimuthal plasma currents can be induced with significantly lower current and voltage transients than otherwise, allowing for less stress to power processing circuitry, thereby increasing thruster lifetime.

B. Relating Results to Other Measurements

The main performance result from this work is the Lorentz force calculation. Ideally, the RMF thruster primarily depends on the Lorentz force to accelerate the plasma, and thus the measured currents and magnetic fields should interact to reproduce experimental performance measurements. Unfortunately, we do not have published performance results for this operating condition, as our published direct thrust stand measurement to-date has used 200 μs pulses rather than the 125 μs pulse from this study. However, performance results for the 125 μs pulses have been taken, and the yet-unpublished result for the operating condition examined in this study is a thrust of 9.7±1.7 mN at a repetition rate of 155 Hz. Even when we discount the erroneous negative current which is measured after the pulse has ended, we find that the calculated axial Lorentz force results in an anticipated thrust of only 64% of what is measured. A strong possibility to explain the gap between measured and actual performance is thermal expansion. The shape of the magnetic bias field is similar to that of a magnetic nozzle, and we could expect thermal expansion to do work to accelerate the plasma as it exits the cone. It can be shown that in the case of an FRC with radial force balance in an expanding magnetic field,

$$\Delta v = \sqrt{\frac{5}{m_i} \left(k_B T_1 - k_B T_2 \right)}, \tag{29}$$

where v refers to ion velocity, m to ion mass, T to electron temperature, and the subscript 2 refers to a downstream position while 1 refers to upstream [7]. Given the low performance we have seen from this thruster in the past [12], it is not unreasonable that thermal and Lorentz based acceleration both contribute in significant portions. However, given that this particular thruster is not designed to leverage thermal effects, it is likely that this type of expansion does not occur as dramatically as it could in an ideal configuration.

We can also examine the radial component of the Lorentz force. We note that there is significant radial force, with the instantaneous magnitude nearly doubling that of the axial force, and with the net impulse nearly quadrupling it. With this being said, we do not see dramatic compression of the plasmoid we might expect given this net force. Rather, the plasmoid appears stable, and remains near the outer edge of the cone for the duration of its lifetime. One possible

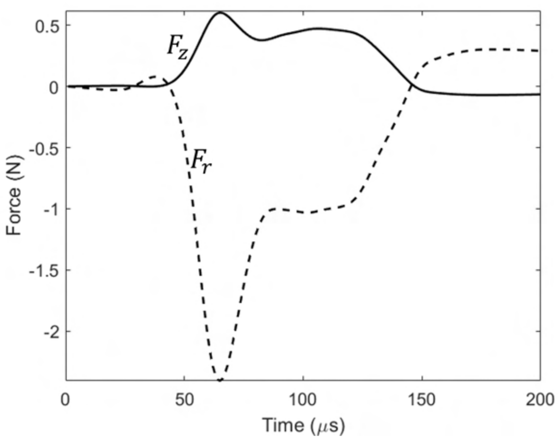

(a)

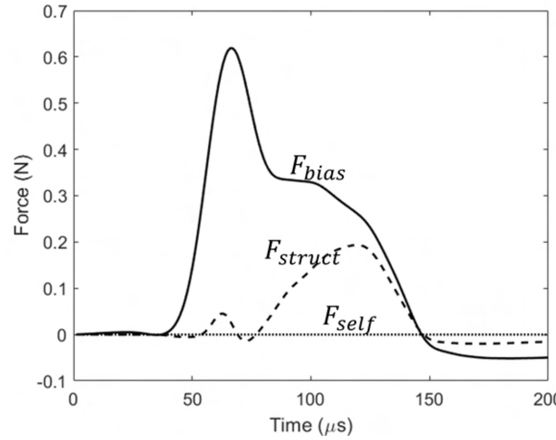

(b)

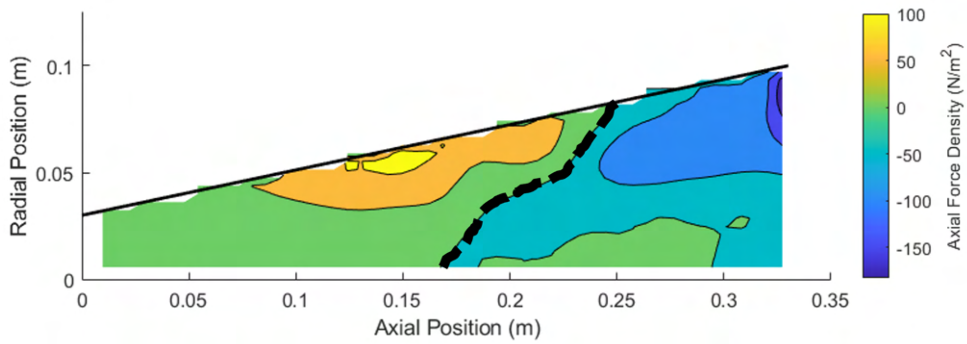

(c)

Fig. 8 Lorentz force experienced by the plasma. a) Net Lorentz forces separated by direction (axial and radial). b) Net axial forces, separated by magnetic field source. c) Axial force density in the r-z plane due to self field only at 70 μs. Thick dashed contour indicates border between positive and negative force regions.

explanation is pressure balance with thermal expansion. If this is the case, we would expect the magnetic pressure to be equal to the electron thermal pressure inside the plasmoid. Analytically, this would mean

$$P_{therm} = P_{mag} \tag{30}$$

$$n_e k_B T_e = \frac{B^2}{2\mu_0} \tag{31}$$

for electron density n_e and temperature T_e, while B refers to the total magnetic field. As an example we can examine the 100 μs time step, where peak magnetic pressure is calculated at ~18 Pa. Indeed, we find in a study by Gill yet to be published that at this same location and time, we measure $n_e = 1.4 \times 10^{1}9$ 1/m^3, and $T_{ev} = 8.8$ eV, for a total outward thermal pressure of 12.32 Pa. That these measurements are of similar magnitude provides strong evidence that this radial force balances the thermal pressure during the time the plasmoid persists, and lends credence to the hypothesis that both thermal and magnetic effects are significant to the operation of the RMF thruster.

C. Implications for Thruster Scaling

One of the most significant results presented above is the lack of any direct self field contribution to axial thrust, as seen in Figure 8b. As discussed in Section III, this can be explained by conservation of momentum. The self field as formulated here involves the current density in one section of the plasma interacting with the magnetic field induced by currents elsewhere in the plasma. In other words, it is the plasma pushing off itself. Because no stationary object is involved in this interaction, there should be no change in the plasma's center of mass. That being said, radial force does not accelerate the plasma's center of mass and thus we can expect to see nonzero radial self field, which we do observe. Barring any additional changes to the thruster, the self field would only be capable of producing acceleration via wall interaction. It could be envisioned that radial outward pressure against the walls could be converted to axial force via the slanted nature of the walls.

Given the self field's non-direct contribution to thrust, we are left with the structure field providing the only direct source of quadratic thrust/current scaling. This structure force could be enhanced via the flux conserver, a design feature present in all fusion-based RMF devices as well as some RMF thrusters. Flux conservers consist of conductive rings which surround the plasma-bounding volume of the thruster, and which serve to couple to the plasma via mutual inductance to produce a structure magnetic field. Flux conservers are critical to the pressure balance in an FRC plasmoid because the structure force serves to bolster the inward magnetic pressure to combat thermal expansion in the hot dense plasmoid, and the conductivity of flux conservers is considered an important figure of merit in the fusion FRC community [21]. For this reason, the addition of flux conservers may also serve to more efficiently convert thermal energy into thrust by applying stronger radial magnetic pressure. The increased radial pressure would lead to acceleration due to the axial asymmetry of the cone, squeezing the plasmoid out toward the open end via pressure gradients.

We have previously dismissed flux conservers due to analytic circuit analysis which suggests that the structure force is inherently inefficient for axial acceleration [17]. Based on those analytic results, we have designed and built the PEPL RMFv2 while minimizing conductive elements to couple to the plasma. The bias magnets remain the only significant flux conserving structural elements in the RMFv2, and we suspect that they are responsible for the measured structure field in this thruster. Given the significance of the structure field even without any intentional flux conservers, a study into the effect of additional flux conserving surfaces on the structure force is warranted if we wish to understand how to increase the portion of thrust scaling which is quadratic with plasma current.

The inefficiency associated with structure force acceleration may be mitigable by use of inductive recapture circuitry. The fundamental efficiency loss for the structure field, disregarding circuit nonidealities such as resistance and stray mutual inductance, is that the structure field generation requires the coupling of energy into the thruster structure. Because of the geometric nature of mutual inductance, it is not possible to fully re-extract that energy in the form of Lorentz force on the plasma. However, one could envision a circuit which is capable of recapturing the inductive energy leftover in the flux conserves by using it to charge a capacitor. This approach has been suggested and implemented for the main antenna in theta-pinch style pulsed inductive thrusters [22][23], but has not been applied to flux conservers to our knowledge.

VIII. Conclusion

In this work, we sought to take direct inductive probe measurements to examine the current drive and Lorentz force mechanism in an RMF thruster. To that end, we designed and built a 2-axis B-dot probe and took measurements during thruster operation throughout the thruster's cross section. Using these results, we were able to establish the efficacy of the RMF current drive mechanism, directly observe FRC formation and acceleration in the thruster, and examine various Lorentz force contributions in the thruster. We found that despite textbook FRC plasmoid formation, axial Lorentz force underpredicts thrust, leading us to believe thermal effects may play a significant role in this device. We also discovered that Lorentz force interaction with the self-field, the magnetic field associated directly with the azimuthal plasma currents, provides no net axial impulse and only serves to expand the plasmoid. The structure field, however, which is associated with currents in conductive elements in the thruster induced by the plasma, does provide a net positive acceleration which scales quadratically with induced plasma currents. The addition of flux conserving rings may serve to increase the magnitude of the structure force, and further research into their implementation is warranted to capitalize on this quadratic scaling.

Acknowledgments

We would like to acknowledge NSTRF Grant 80NSSC18K1190 and NSTGRO Grand 80NSSC20K1168 which supported this work. The power supply was developed as part of an SBIR award with Eagle Harbor Technologies, and additional funding was granted by AFOSR Grant FA9550-19-1-0022 from the Space Propulsion and Power portfolio.

References

[1] Polzin, K., Martin, A., Little, J., Promislow, C., Jorns, B., and Woods, J., "State-of-the-Art and Advancement Paths for Inductive Pulsed Plasma Thrusters," *Aerospace*, Vol. 7, No. 8, 2020, p. 105.

[2] of Sciences Engineering, N. A., and Medicine, *Space Nuclear Propulsion for Human Mars Exploration*, The National Academies Press, Washington, DC, 2021. https://doi.org/10.17226/25977, URL https://www.nap.edu/catalog/25977/space-nuclear-propulsion-for-human-mars-exploration.

[3] Vitug, E., "Lunar Surface Innovation Initiative (LSII)," , Jul 2020. URL https://www.nasa.gov/directorates/spacetech/game_changing_development/LSII.

[4] Blevin, H. A., and Thonemann, P. C., "Plasma confinement using an alternating magnetic field," *Nuclear Fusion Supplement, Part 1*, 1962, p. 55.

[5] Jahn, R. G., *Physics of Electric Propulsion*, McGraw-Hill Book Company, New York, 1968.

[6] Slough, J., Kirtley, D., and Weber, T., "Pulsed plasmoid propulsion: The ELF thruster," *31th International Electric Propulsion Conference*, 2009, pp. 20–24.

[7] Weber, T. E., "The Electrodeless Lorentz Force Thruster Experiment," Ph.D. thesis, University of Washington, 2010.

[8] Kirtley, D., Pancotti, A., Slough, J., and Pihl, C., "Steady operation of an FRC thruster on Martian atmosphere and liquid water propellants," *48th AIAA/ASME/SAE/ASEE Joint Propulsion Conference & Exhibit*, 2012, p. 4071.

[9] Furukawa, T., Takizawa, K., Kuwahara, D., and Shinohara, S., "Electrodeless plasma acceleration system using rotating magnetic field method," *AIP Advances*, Vol. 7, No. 11, 2017, p. 115204.

[10] Furukawa, T., Takizawa, K., Yano, K., Kuwahara, D., and Shinohara, S., "Spatial measurement in rotating magnetic field plasma acceleration method by using two-dimensional scanning instrument and thrust stand," *Review of Scientific Instruments*, Vol. 89, No. 4, 2018, p. 043505.

[11] Furukawa, T., Shimura, K., Kuwahara, D., and Shinohara, S., "Verification of azimuthal current generation employing a rotating magnetic field plasma acceleration method in an open magnetic field configuration," *Physics of Plasmas*, Vol. 26, No. 3, 2019, p. 033505.

[12] Sercel, C. L., Gill, T., Woods, J. M., and Jorns, B., "Performance Measurements of a 5 kW-Class Rotating Magnetic Field Thruster," *AIAA Propulsion and Energy 2021 Forum*, 2021, p. 3384.

[13] Gill, T., Sercel, C. L., Woods, J. M., and Jorns, B. A., "Experimental Characterization of Efficiency Modes in a Rotating Magnetic Field Thruster," *AIAA SCITECH 2022 Forum*, 2022, p. 2191.

[14] Jones, I. R., and Hugrass, W. N., "Steady-state solutions for the penetration of a rotating magnetic field into a plasma column," *Journal of Plasma Physics*, Vol. 26, No. 3, 1981, pp. 441–453.

[15] Jones, I. R., and Hugrass, W. N., "Steady-state solutions for the penetration of a rotating magnetic field into a plasma column," *Journal of Plasma Physics*, Vol. 26, No. 3, 1981, pp. 441–453.

[16] Viges, E. A., Jorns, B. A., Gallimore, A. D., and Sheehan, J., "University of Michigan's Upgraded Large Vacuum Test Facility," *36th International Electric Propulsion Conference*, 2019.

[17] Sercel, C. L., Woods, J. M., Gill, T., and Jorns, B., "Impact of Flux Conservers on Performance of Inductively Driven Pulsed Plasmoid Thrusters," *AIAA Propulsion and Energy 2020 Forum*, 2020, p. 3632.

[18] Polzin, K. A., Hill, C. S., Turchi, P. J., Burton, R. L., Messer, S., Lovberg, R. H., and Hallock, A. K., "Recommended practice for use of inductive magnetic field probes in electric propulsion testing," *Journal of Propulsion and Power*, Vol. 33, No. 3, 2017, pp. 659–667.

[19] Sandwell, D. T., "Biharmonic spline interpolation of GEOS-3 and SEASAT altimeter data," *Geophysical research letters*, Vol. 14, No. 2, 1987, pp. 139–142.

[20] Martin, A., and Eskridge, R., "Electrical coupling efficiency of inductive plasma accelerators," 2005. https://doi.org/10.1088/0022-3727/38/23/005.

[21] Myers, C., Edwards, M., Berlinger, B., Brooks, A., and Cohen, S., "Passive Superconducting Flux Conservers For Rotating Magnetic Field Driven Field Reversed Configurations," *Fusion Science and Technology*, Vol. 61, 2012, pp. 86–103.

[22] Bernardes, J., and Merryman, S., "Parameter analysis of a single stage induction mass driver," Tech. rep., NAVAL SURFACE WEAPONS CENTER DAHLGREN VA, 1985.

[23] Polzin, K., Rose, M., Miller, R., Best, S., Owens, T., and Dankanich, J., "Design of a low-energy FARAD thruster," *43rd AIAA/ASME/SAE/ASEE Joint Propulsion Conference & Exhibit*, 2007, p. 5257.